2016

A Method for Thermal Performance Characterization of Ultra-Thin Vapor Chambers Cooled by Natural Convection

G. Patankar

S. Mancin

J. A. Weibel
Purdue University, jaweibel@purdue.edu

M. A. McDonald

S V. Garimella
Purdue University, sureshg@purdue.edu

Follow this and additional works at: http://docs.lib.purdue.edu/coolingpubs

Gaurav Patankar
Cooling Technologies Research Center,
an NSF I/UCRC,
School of Mechanical Engineering,
Purdue University,
585 Purdue Mall,
West Lafayette, IN 47907
e-mail: gpatank@purdue.edu

Simone Mancin
Cooling Technologies Research Center,
an NSF I/UCRC,
School of Mechanical Engineering,
Purdue University,
585 Purdue Mall,
West Lafayette, IN 47907
e-mail: simone.mancin@unipd.it

Justin A. Weibel
Cooling Technologies Research Center,
an NSF I/UCRC,
School of Mechanical Engineering,
Purdue University,
585 Purdue Mall,
West Lafayette, IN 47907
e-mail: jaweibel@purdue.edu

Suresh V. Garimella[1]
Cooling Technologies Research Center,
an NSF I/UCRC,
School of Mechanical Engineering,
Purdue University,
585 Purdue Mall,
West Lafayette, IN 47907
e-mail: garimell@purdue.edu

Mark A. MacDonald
Intel Corporation,
5200 Elam Young Pkwy,
Hillsboro, OR 97124
e-mail: mark.macdonald@intel.com

A Method for Thermal Performance Characterization of Ultrathin Vapor Chambers Cooled by Natural Convection

Vapor chamber technologies offer an attractive approach for passive cooling in portable electronic devices. Due to the market trends in device power consumption and thickness, vapor chamber effectiveness must be compared with alternative heat spreading materials at ultrathin form factors and low heat dissipation rates. A test facility is developed to experimentally characterize performance and analyze the behavior of ultrathin vapor chambers that must reject heat to the ambient via natural convection. The evaporator-side and ambient temperatures are measured directly; the condenser-side surface temperature distribution, which has critical ergonomics implications, is measured using an infrared (IR) camera calibrated pixel-by-pixel over the field of view and operating temperature range. The high thermal resistance imposed by natural convection in the vapor chamber heat dissipation pathway requires accurate prediction of the parasitic heat losses from the test facility using a combined experimental and numerical calibration procedure. Solid metal heat spreaders of known thermal conductivity are first tested, and the temperature distribution is reproduced using a numerical model for conduction in the heat spreader and thermal insulation by iteratively adjusting the external boundary conditions. A regression expression for the heat loss is developed as a function of measured operating conditions using the numerical model. A sample vapor chamber is tested for heat inputs below 2.5 W. Performance metrics are developed to characterize heat spreader performance in terms of the effective thermal resistance and the condenser-side temperature uniformity. The study offers a rigorous approach for testing and analysis of new vapor chamber designs, with accurate characterization of their performance relative to other heat spreaders. [DOI: 10.1115/1.4032345]

Introduction

A heat pipe or vapor chamber can passively transport heat from a localized generation source to a diffuse heat rejection surface at a low temperature gradient. There is an extensive body of research on the investigation of heat pipes and vapor chambers for the thermal management of electronics [1]. A vapor chamber is used to mitigate the temperature rise of sensitive components by spreading heat away from local hot spots. The sealed vapor chamber contains a working fluid, and vapor is generated at the evaporator section located over the hot spot. The vapor is driven outward and condenses on the inner surface of the opposing wall. A porous wick passively pumps the condensed liquid back to the evaporator (Fig. 1). Portable electronic device platforms such as smartphones and tablets are trending toward thinner, compact designs with more embedded functionality (and thereby more waste heat generation from active components). Due to power consumption and

size constraints, it is not practical to use active air cooling methods, or heat rejection surfaces with large area enhancement, to dissipate heat. In such instances, ultrathin vapor chambers may offer a viable solution.

Prior studies have experimentally assessed the performance of heat pipes and vapor chambers using a standard testing approach in which the heat is spread from a heat source to a cold plate or air-cooled heat sink, and the heater-to-ambient thermal resistance is determined [2]. The transport behavior of internal components of a vapor chamber, such as the effective thermal resistance across
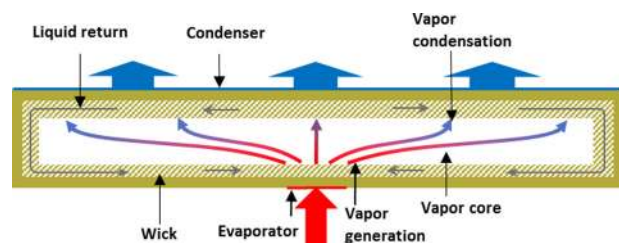

Fig. 1 Schematic diagram of vapor chamber operation

---

[1]Corresponding author.
Contributed by the Electronic and Photonic Packaging Division of ASME for publication in the JOURNAL OF ELECTRONIC PACKAGING. Manuscript received September 12, 2015; final manuscript received November 16, 2015; published online March 10, 2016. Assoc. Editor: Ashish Gupta.

the evaporator wick [3,4], can also be assessed. In a testing configuration closely related to the current study, Wang et al. [5] investigated copper vapor chambers that contained interlaced grooves and channels as the wick structure. The hot spot heat input was supplied through a copper platen with an embedded rake of thermocouples for heat flux measurement. Heat was rejected on the condenser side using a finned heat sink cooled by forced air convection. Thermal grease was used to reduce contact resistance between the vapor chamber and the heat sink; thermocouples were embedded in this grease layer between the heat sink and the vapor chamber to measure surface temperatures. The thermal performance of the vapor chamber was assessed based on its thermal resistance and condenser-side temperature uniformity [5]. This vapor chamber testing configuration has commonly been used [6–9]. Other variants use a liquid-cooled cold plate on the condenser side [10]. This testing configuration is tailored for high-power or high-density cooling applications for which the heat flux induces a large temperature gradient in the heater platen that can be accurately measured, and where the condenser-side heat rejection method mimics the intended application. For example, Mochizuki et al. [9] tested input heat fluxes from 20 to 100 W over 1 cm^2, Wong et al. [6] from 300 to 400 W over ~1–4 cm^2, and Chen et al. [8] from 20 to 80 W over ~2 cm^2. The lowest reported heat fluxes investigated under this vapor chamber testing configuration include measurements by Koito et al. [11] from 16 to 32 W/cm^2 and Wang et al. [5] from ~4 to 10 W/cm^2.

In portable electronic platforms, heat is rejected to the ambient via natural convection directly from the device surface (typically a smooth, flat surface that does not incorporate a finned heat sink due to lack of space and the low operating power). Hence, it is necessary to develop good characterization techniques for vapor chambers cooled by natural convection. To the authors' knowledge, experimental investigation of vapor chambers operating at a low power density where the condenser-side boundary condition is one of natural convection has not been considered in the literature. Also, due to the proximity of the vapor chamber condenser surface to the device skin in thin form factor platforms, an assessment of the condenser-side surface temperature *distribution* is extremely important. This product sector necessitates a paradigm shift in thermal management, where the external surface temperature threshold is dictated by user considerations, rather than by device operating temperature limits. According to Moritz and Henriques [12], roughly 5 mins of contact with temperatures of ~50 °C can cause skin tissue damage; to avoid this condition, performance throttling would be dictated by user comfort standards. Berhe [13] defined ergonomic temperature limits on handheld devices of 41 °C for aluminum surfaces and 43 °C for plastic surfaces. It is clear from this review that existing metrology approaches stress a characterization of the total thermal resistance of the vapor chamber, while few studies analyze the condenser-side temperature distribution. A rigorous mapping of the surface temperature distribution is necessary to characterize vapor chamber performance for portable electronics applications.

This paper presents an approach for characterizing the performance of ultrathin vapor chambers for portable electronics platforms operating at low power. An experimental test facility is developed that subjects the vapor chamber to a hot spot on the evaporator side and rejects heat from the condenser side by natural convection. Precise evaluation of performance at very low power densities (~1 W/cm^2) is enabled by a combined experimental and numerical approach for calibration of the heat transport through the vapor chamber. Keeping the heat source at the minimum possible temperature and mitigating hotspots on the condenser surface are key functional requirements. Hence, in addition to the conventional thermal resistance metric, IR measurement of the condenser-side surface temperature allows characterization of the vapor chamber performance in terms of temperature distribution. The assessment is based on the performance of an ultrathin vapor chamber relative to a solid heat spreader with identical outer dimensions.

Experimental Facility

An experimental facility is developed to evaluate the performance of ultrathin vapor chambers at low heat loads. The intrinsic challenge in vapor chamber characterization under such conditions is estimation of the percentage of heat input rejected through the vapor chamber versus parasitic losses through other pathways. To measure extremely low heat loads, a test section is typically designed to eliminate heat losses (an isolated system, e.g., Ref. [2]). To evaluate performance of a vapor chamber rejecting heat to the ambient via natural convection, which inserts a large associated thermal resistance in the primary heat rejection pathway, it is difficult to create a sufficiently isolated system. An alternative approach is to control the heat losses in a manner that allows for accurate estimation and calibration, as implemented in the current study.

Test Section Design and Instrumentation. A schematic diagram of the test section configuration is shown in Fig. 2. The test section is comprised of the heat spreader sample, with insulation and a centered heater block on the underside; the top side of the heat spreader is exposed to ambient air. The test section insulation is made of PEEK ($k = 0.25$ W m^{-1} K^{-1}) with outer dimensions of 150 mm × 115 mm × 25.4 mm. A 92 mm × 52 mm × 0.7 mm deep recess milled into the top surface of the insulation seats the heat spreader sample. In the center, a 10 mm × 10 mm square pocket was machined to insert the heater block assembly. As shown in the inset of Fig. 2, the hot spot heat input is simulated using a 10 mm × 10 mm thin-film polyimide heater attached using thermally conductive paste to the base of a 10 mm copper heater block that ensures uniform distribution of the heat load imposed on the spreader. A uniform, thin layer of high-conductivity epoxy was applied onto the bottom surface of the heat spreader to cover the area overlapping the copper heater block. This allowed a consistent joint to be formed between the heat spreader and heater block across all samples to yield consistent calibration. The top surface of the vapor chamber is cooled by natural convection to the surrounding air.

A photograph of the experimental facility is shown in Fig. 3. A sample is shown inserted into the test section, and the auxiliary components for temperature and power measurements are visible.

The spatial temperature distribution on the top surface of the heat spreader is measured by a mid-wave IR camera (Indigo
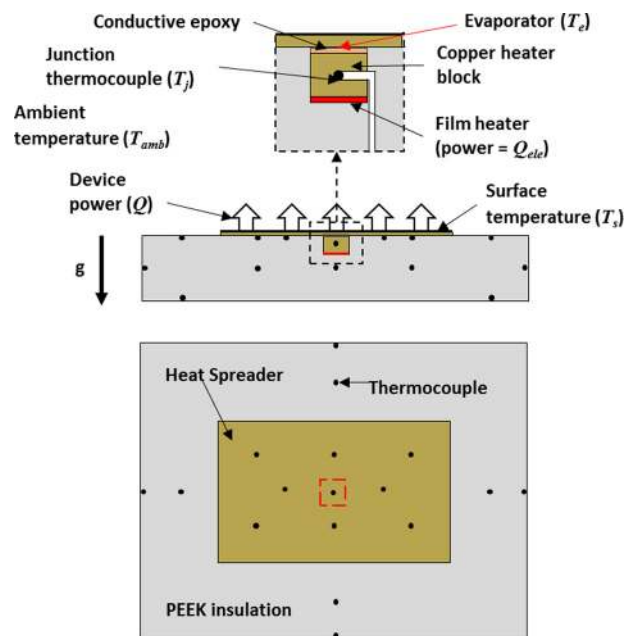

Fig. 2 Schematic diagram of the test section (top inset shows the heater block assembly)
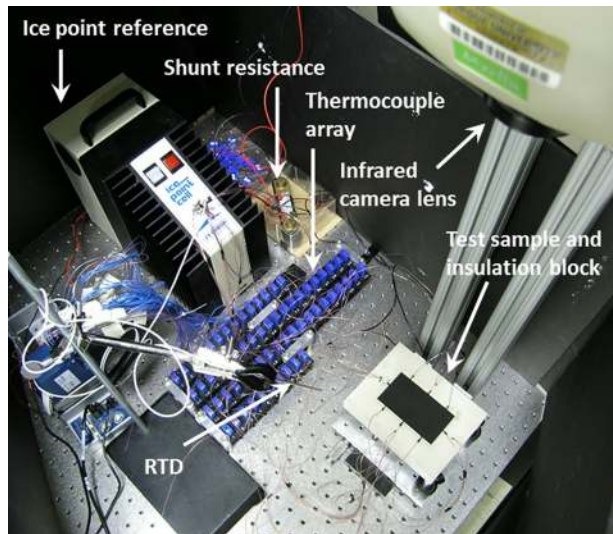
Fig. 3 Photograph of the experimental facility

Merlin MID, FLIR) positioned above the test section. Visualization of the surface temperature via an IR camera allows for the development of performance metrics based on the surface temperature distribution. Calibration of the IR camera measurement was carried out using a reference black body (Blackbody Source Model 2004, SBIR) with a known emissivity (0.985 ± 0.015). The temperature of the black body was incremented in steps of $5\,°C$ from $20\,°C$ to $100\,°C$. From the recorded images, a pixel-by-pixel calibration of the surface temperature versus sensor output was performed. A sixth-order polynomial curve was fit to the data to obtain a correlation between sensor output and temperature. Subsequent evaluation of the calibration at selected blackbody reference temperatures in the $20\,°C$ to $100\,°C$ range showed a maximum mean error averaged over the field of view of $0.2\,°C$. The top surface of the heat spreader sample is painted black (#1602, Krylon) to impart a known emissivity of 0.96 [14]; the ratio of the calibration black body emissivity to the surface emissivity is used to correct the IR temperature measurement.

As shown in Fig. 2, a total of 30 thermocouples are embedded throughout the insulation block to monitor the temperature. In particular, the thermocouple locations are classified into groupings of those embedded under the top, side, and bottom surfaces (four each) and in the middle of the insulation block (nine). Eight thermocouples are placed in grooves along the surface in contact with the bottom of the heat spreader. Finally, a thermocouple is inserted at the center of the copper heater block to measure the junction temperature. This deployment of thermocouples is essential to the calibration procedure used for estimation of the heat loss from the insulation block, as described in the following section. Each thermocouple was individually wired to a reference junction that is placed in a dry-block ice point reference (TRCIII, Omega). The thermocouples were individually calibrated using a thermostatic oil bath (7103 Micro-Bath, Fluke) and two factory-calibrated resistance temperature detectors (RTD, $\pm 0.1\,K$), one each for the ice point and the oil bath. Following calibration, the thermocouple temperature measurements have an absolute uncertainty of $\pm 0.3\,K$. The ambient temperature is measured using an RTD.

The electrical power supplied to the film heater is determined by measuring the voltage drop across the resistance heating element and across a shunt resistance placed in series with the film heater. The electrical input power has a measured uncertainty of 0.2% (governed by the shunt resistance uncertainty).

Test Procedure. A strict experimental procedure is followed for all tests to ensure repeatability of the measurements. The IR camera is switched on at least $1\,hr$ prior to starting the test to ensure that the sensor cools down to a steady temperature for

reduced noise in the images. Boards are placed around the test section so as to prevent air flow disturbances in the surrounding ambient. To acquire each data point, the electrical power input to the heater is set at the desired value; all the monitored data are recorded every $4\,s$ using an NI cDAQ 9178 data acquisition chassis with NI 9124 thermocouple, NI 9217 RTD, and NI 9205 voltage input modules. Active data processing is performed in a LABVIEW interface to determine when steady-state conditions have been reached, defined as when the standard deviation of the junction temperature for the last 150 data points is less than $0.02\,K$. The time usually taken to reach steady-state conditions is approximately $3\,hrs$. After steady-state conditions are reached, the performance is monitored for an extended period (~ 30 min) to obtain a large steady-state data set; IR images are acquired at 5-min intervals during this period. Due to the small fluctuations in ambient temperature that affect the test section temperatures at steady state, a set of 150 data points is selected from the steady-state data set which has the lowest standard deviation in junction temperature. An average over these data is used for subsequent analysis, and associated with the specific steady-state IR image taken during this interval. This procedure for acquiring a single data point is repeated for each heat input power.

Calibration of the Test-Section Heat Loss

A calibration procedure is implemented that predicts heat loss from the test section. The experimental step of the calibration procedure evaluates heat spreading in two thin metal plates of known thermal conductivity, viz., copper and aluminum. The test section temperatures were recorded for heat loads in the nominal range of 0.15–4 W. Key characteristics of the metal heat spreaders used for the calibration process are listed in Table 1.

A numerical model of the test section is generated to simulate conduction in the heater block assembly, insulation block, and heat spreader. As shown in Fig. 4, the model boundary conditions have a constant heat flux applied at the base of the heater block, a thermal resistance at the interface between the insulation and heat

Table 1 Heat-loss calibration data set

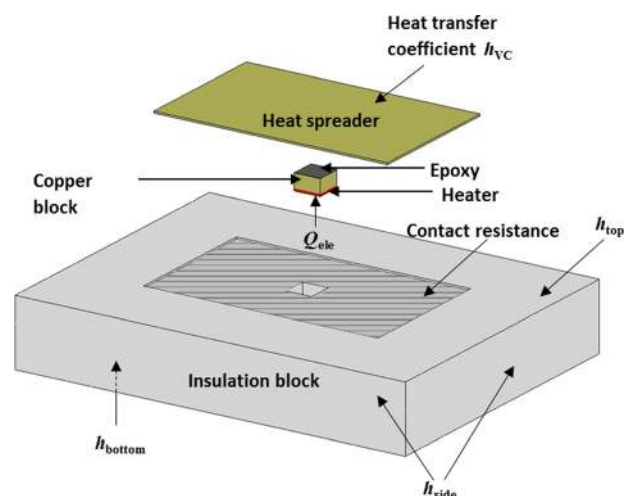|	Copper	Aluminum
Thermal conductivity (W m^{-1} K^{-1})	387.6	202.4
Outer dimensions (mm)	$90 \times 55 \times 0.7$	$90 \times 51 \times 0.635$
Electrical heat input (W)	0.17–4.16	0.16–3.88
# of data points	8	10

Fig. 4 Exploded view of the numerical conduction model domain and boundary conditions

spreader, and convection coefficients on each external surface. A grid-independent rectangular mesh is used to discretize the geometry using a total of ~325,000 cells. The peripheral regions of the insulation block have a uniform coarse mesh; the solution is insensitive to further refinements because of the low temperature gradients in these regions. The copper heater block assembly has a finer mesh. In the heat spreader, a gradient-based mesh is used for refinement near the hotspot. The lateral cell lengths increase in the outward direction from 0.25 mm to 2.25 mm. There are 20 cells across the thickness of the heat spreader near the hotspot. The properties of the heat spreader are specified for the sample being tested according to Table 1. The governing energy equation is solved using the finite-volume method implemented in the commercial software ANSYS FLUENT [15].

The primary objective of the numerical model is to predict the boundary conditions and overall heat losses that cannot be determined directly from the available experimental data. A formal procedure is implemented in order to iterate on the boundary conditions in the model in order to produce good agreement between the experimental and numerical values of temperature at the locations in the test section measured by thermocouples. For each calibration data point, the free variables in the numerical simulation are the heat transfer coefficients on the top, side, and bottom surfaces of the insulation block and the heat spreader top surface. Tuning of the thermal resistance at the interface between the insulation and heat spreader to a fixed value of 0.02 m^2 K W^{-1} across all test cases yielded the best agreement with experimental data (equivalent to an air gap thickness of 0.5 mm).

For the initial guess value, a prediction of the natural convection heat transfer coefficient at each surface with a different orientation obtained from standard correlations was imposed, and then was subsequently iterated to generate a match with the thermocouple data. Priority was given to first match the junction temperature closest to the heat source, and then finer adjustments to the boundary heat transfer coefficients (increments of 0.5 W m^{-2} K^{-1}) were made to minimize the overall average deviation from the experimental temperature data. Simple rules were applied that ensure the heat transfer coefficients increased from the downward to upward facing surfaces according to the physical behavior expected. With a sufficient match to the experimental data, the heat transported through the heat spreaders and the heat loss through the insulation block can be easily extracted from the numerical data.

The values of the external heat transfer coefficients were found to be in the range from 4 to 16 W m^{-2} K^{-1}. In the current study, where low heat loads are applied and the overall heat loss is a significant percentage of the overall heat input, a single value for the heat transfer coefficient on all exposed surfaces did not yield sufficient accuracy in the match between experimental and numerical temperatures. When these values were allowed to independently vary, the temperature mismatch between the measured and computed values was significantly decreased for all test cases.

The temperature mismatch between the test and the simulation, averaged over all the cases, is 0.34 K, with a standard deviation of 0.56 K. Figure 5 shows a comparison between the simulated temperatures after iterating on the boundary conditions compared with the measured values for a selected copper spreader test case. The thermocouple groups (as discussed under "Test Section Design and Instrumentation" section) are on the bottom, side, and top surfaces of the insulation block, inside the insulation block (internal), embedded below the heat spreader, and at the junction. For the selected case, the junction temperature is matched most closely (difference of 0.02 K); the maximum difference is observed for the heat spreader group of thermocouples (difference of 0.71 K).

Using this calibration procedure, the uncertainty in the evaluated heat loss from the test section is roughly estimated based on both the resolution of the heat transfer coefficient increments used during the iteration process and the ultimate temperature mismatch at the surface-embedded thermocouple locations. Using these component uncertainty values for each case, and expressing the heat loss as a single equation of the form
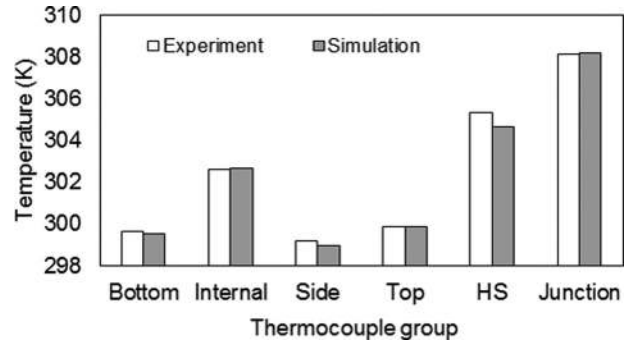
Fig. 5 Comparison of thermocouple temperatures obtained from experiments against those from the simulations at an electrical heat input of 1 W and ambient temperature of 298.2 K. Each bar is an average temperature from each grouping of thermocouples.

$$Q_{loss} = h \times A \times (T - T_{amb}) \qquad (1)$$

a standard propagation of errors can be used estimate the uncertainty in the predicted heat loss; this uncertainty varies from 3% to 14% of the calculated heat loss for the test cases described in Table 1.

The heat loss values extracted from the calibration of the copper and aluminum heat spreaders are plotted in Fig. 6(a). A generalized regression is developed for the heat loss value as a function of the electrical input power and the junction-to-ambient temperature difference, as given by

$$Q_{loss} = \left[a \times \left(\frac{T_j - T_{amb}}{Q_{ele}} \right)^b \right] Q_{ele} \qquad (2)$$

This form of the equation assumes that the heat loss value is proportional to the electrical input power (and that there is no heat loss at zero input power). This relationship can be clearly observed in Fig. 6(a) (dashed lines indicate best linear fit to the data points). The proportionality constant would then depend on the thermal resistance of the sample being tested. The ratio of junction-to-ambient temperature difference and the electrical input reflects this thermal resistance. By evaluating the thermal resistance of both the copper and aluminum heat spreaders, as shown in Fig. 6(b), the influence of the junction-to-ambient temperature on the overall heat loss can be incorporated into the regression. The result of the calibration yields the constants $a = 0.14$ and $b = 0.57$, which can subsequently be used to calculate the heat losses through the insulation block when evaluating heat spreading devices that have an unknown thermal resistance and heat spreading behavior. The values of these constants are specific to the current test section design; a similar calibration procedure would need to be employed with any change in the experimental setup.

Results and Performance Metrics

A representative vapor chamber device with outer dimensions of 90 mm × 50 mm × 0.8 mm, obtained from a commercial vendor, is characterized to demonstrate the testing approach developed. The copper vapor chamber has 0.2-mm-thick copper walls, uses water as the working fluid, and is lined with a single layer of copper mesh (pore sizes of approximately 50–100 μm). The heat spreading behavior of the vapor chamber is evaluated for 12 device power levels (electrical heat input minus losses) ranging from 0.4 to 2.2 W, and resulting in vapor chamber area-weighted mean condenser-side surface temperatures from 24.2 °C to 50.3 °C, and maximum condenser-side surface temperatures in the range of 32.8 °C to 55.9 °C. During testing, the ambient air
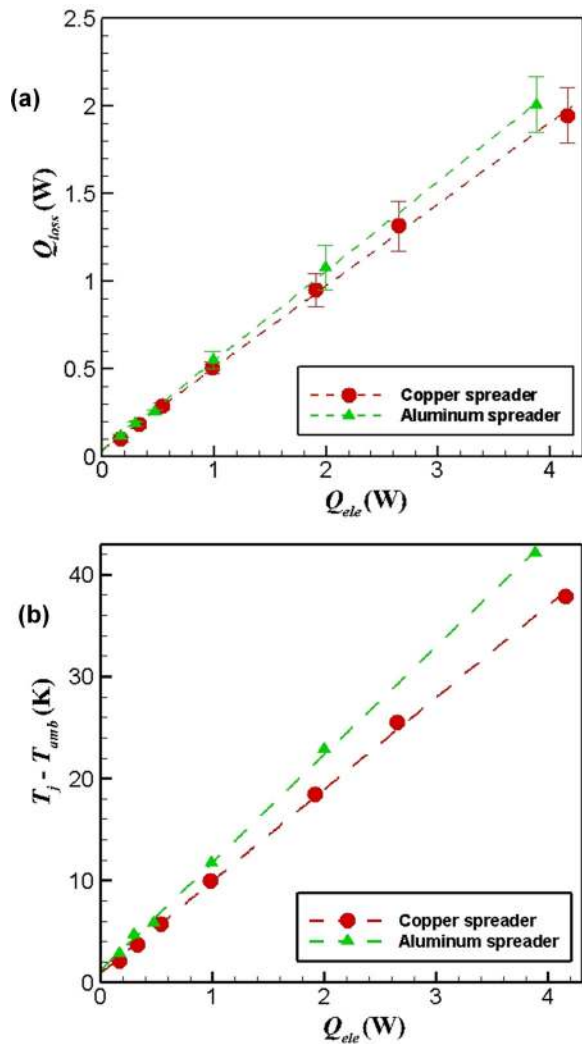
Fig. 6 (a) Calibrated numerical model estimates of the heat loss and (b) junction-to-ambient temperature differences, as a function of input power for the copper and aluminum heat spreaders

temperature fluctuated from 22.2 °C to 24.0 °C. The data obtained from the tests were used to assess the behavior of the vapor chamber relative to the solid copper heat spreader of the same dimensions.

The key functional requirements of the vapor chamber are to keep the heat source at the lowest possible temperature and to mitigate any hot spots in the temperature profile on the condenser side for ergonomic comfort. Performance metrics are proposed based on these criteria as a standard approach to evaluating and comparing between thin vapor chambers and alternative heat spreader designs.

Device Thermal Resistance. A common metric used for defining the thermal resistance of heat pipes and vapor chambers is the junction-to-ambient temperature rise as a function of device power [9]. However, the large thermal resistance contributed by the condenser-side natural convection (in addition to the comparatively smaller thermal resistances of the copper block and conductive epoxy layer) should be omitted from the device thermal resistance assessment for the current configuration, since its inclusion would mask any variations in performance of the actual device under test. The device thermal resistance is instead characterized using the difference between the evaporator temperature (T_e) and the area-averaged condenser-side surface temperature
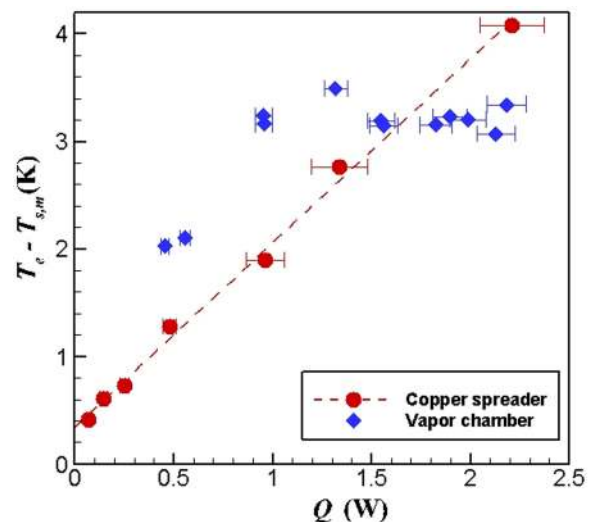
($T_{s,m}$) shown as a function of heat input for the vapor chamber and copper spreader in Fig. 7. The uncertainty in device power is the same as the computed heat loss (uncertainty in the electrical input power is negligible). The constant intrinsic thermal conductivity of the copper heat spreader yields a linear behavior. The vapor chamber performance is nonlinear and shows a crossover at approximately 1.5 W, above which it performs better than the copper heat spreader. One reason for this nonlinear behavior for the ultrathin vapor chamber tested can be attributed to its governing transport mechanism. The predominant contribution to the temperature rise across the vapor chamber is the vapor-core temperature gradient (related to the vapor pressure gradient via the Clausius–Clapeyron relation). Hence, for ultrathin vapor chambers, the thermal resistance relative to a solid heat spreader is governed by the vapor temperature gradient, as shown by Yadavalli et al. [16]. The vapor figure of merit defined in Ref. [16] captures this effect and increases with operating temperature for water; thus, a performance increase with power input, which raises the vapor chamber mean temperature, is expected.

Surface Temperature Distribution. A surface temperature-related spreading metric is developed to characterize the condenser-side temperature profile of the vapor chamber for ergonomics considerations. The contour plot in Fig. 8 shows the condenser side temperature (T_s) distributions for the copper heat spreader and vapor chamber for two different heat input powers selected to be above and below the thermal resistance crossover. For the power input above the performance crossover, the vapor chamber qualitatively exhibits better spreading as compared to the copper spreader (as indicated by the reduced contour color gradient). This characteristic is captured by a surface spreading performance metric as developed below.

The condenser-side surface temperature data obtained from each image pixel are processed to evaluate the surface spreading metric. The difference between the local surface temperature and the mean surface temperature is first normalized by the device heat input as

$$T_{\text{norm}}(x,y) = \frac{\left(T_s(x,y) - T_{s,m}\right)}{Q} \tag{3}$$

Figure 9 shows this value along the center length of the condenser-side surface. For the solid copper spreader, the profile is independent of the heat input power, due to the constant thermal conductivity of copper. The same normalization is then applied to the vapor chamber, for which the profile is seen to flatten with

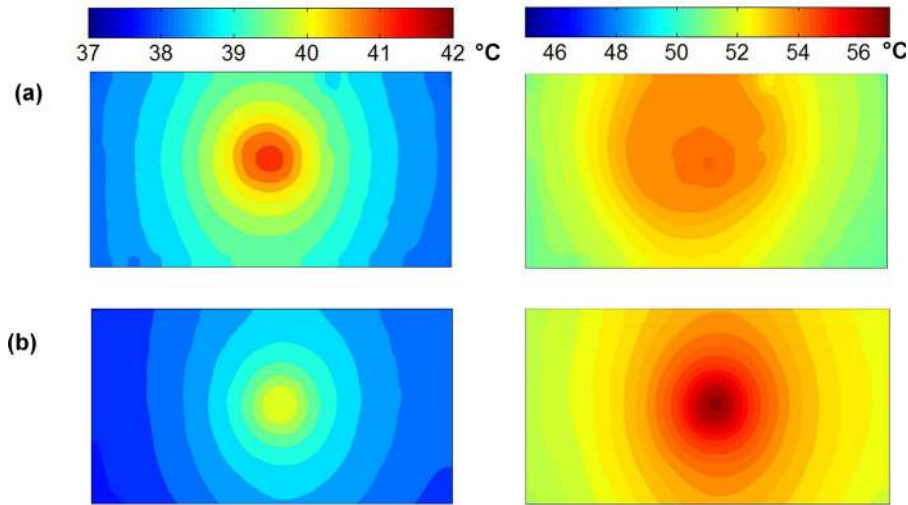Fig. 7 Thermal resistance as a function of power for the solid copper spreader and the vapor chamber

Fig. 8 Contours of the condenser-side surface temperature for the (a) vapor chamber and (b) solid copper spreader at device heat inputs of approximately 1 W (left) and 2 W (right). Note the different temperature scales.
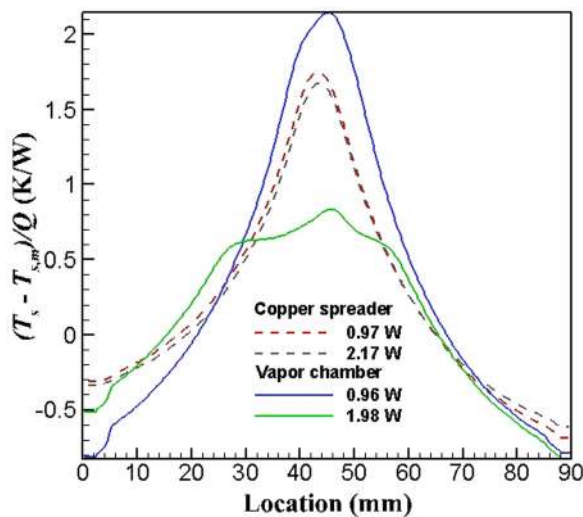

Fig. 9 Condenser-side surface temperature difference from the mean, normalized by the device power (profile drawn along the length of the device passing through the center)

Fig. 10 Spreading metric for the prototype vapor chamber relative to the solid copper heat spreader as a function of device heat input

increasing device power. A measure of the overall temperature uniformity of the condenser-side surface is the inverse of the root mean square value of T_{norm} taken across all pixels. Taking a ratio of this quantity for the vapor chamber to that of the solid copper spreader yields a metric for the surface temperature spreading performance relative to the solid copper spreader

$$\text{Spreading metric} = \frac{\left(1/\text{RMS}\left(\frac{T_s - T_{s,m}}{Q}\right)\right)_{\text{VC}}}{\left(1/\text{RMS}\left(\frac{T_s - T_{s,m}}{Q}\right)\right)_{\text{Cu}}} \quad (4)$$

This metric weighs the relative ability of each heat spreader to affect a uniform condenser-surface temperature profile. For an ideal heat spreader, the temperature profile would be a uniform temperature on the condenser surface at $T_{s,m}$ if the convective boundary condition on the condenser is uniform. The spreading metric would tend to infinity for an ideal heat spreader. The spreading metric results for the vapor chamber tested in the
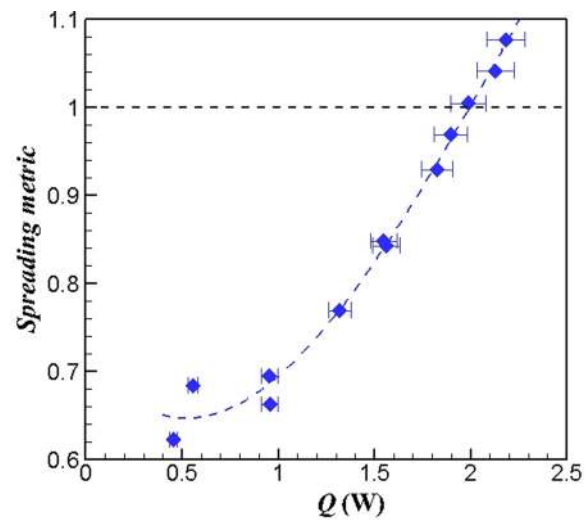
current study are plotted in Fig. 10. A value of 1 indicates that the vapor chamber and the copper spreader perform identically. The plot in Fig. 10 shows an increasing performance of the vapor chamber with increasing power, and a crossover at ~2 W. The spreading metric can be used to compare any heat spreaders of the same dimensions to evaluate the spreading capability.

Conclusions

A novel approach was developed for characterization of vapor chambers of ultrathin form factor. Given their intended application in portable electronics platforms, the experimental facilities are designed to evaluate performance at low heat input powers with heat rejection to the ambient by natural convection. The condenser surface temperature distribution was monitored because of ergonomics implications that govern the thermal management requirements for these applications. The high thermal resistance due to natural convection in the heat dissipation pathway necessitates careful calibration of the parasitic heat losses from the system. A calibration process was developed, which combines experimental and numerical methods to formulate a correlation for the heat loss as a function of surface temperature and electrical input power. A

vapor chamber prototype was tested to demonstrate the metrology developed for characterizing the thermal resistance and condenser-side surface temperature uniformity. Comparing the performance of the vapor chamber to a copper heat spreader using the proposed metrics revealed that vapor chambers may redistribute the condenser-side surface temperature with increasing power, beyond what is possible with heat spreading by conduction alone.

The testing methodology developed is an important tool for the development of vapor chambers and heat spreaders intended for use in portable electronics platforms. Vapor chamber designs can thereby be characterized and compared using a standard approach.

Acknowledgment

Nomenclature

A = area (m^2)
h = convection coefficient (Wm^{-2} K^{-1})
Q = heat input to the heat spreader (W)
Q_{ele} = electrical power (W)
Q_{loss} = heat loss through the insulation (W)
T = temperature (K)

Subscripts

amb = ambient
bottom = PEEK insulation bottom surface
Cu = copper spreader
e = evaporator
j = junction
m = mean
norm = normalized
s = surface
side = PEEK insulation side surface
top = PEEK insulation top surface
VC = vapor chamber

References

[1] Reay, D. A., Kew, P. A., and McGlen, R. J., 2014, *Heat Pipes Theory, Design and Applications*, 6th ed., Butterworth-Heinemann, Oxford, UK, pp. 207–225.
[2] Hopkins, R., Faghri, A., and Khrustalev, D., 1999, "Flat Miniature Heat Pipes With Micro Capillary Grooves," ASME J. Heat Transfer, **121**(1), pp. 102–109.
[3] Davis, T. W., and Garimella, S. V., 2008, "Thermal Resistance Measurement Across a Wick Structure Using a Novel Thermosyphon Test Chamber," Exp. Heat Transfer, **21**(2), pp. 143–154.
[4] Weibel, J. A., Garimella, S. V., and North, M. T., 2010, "Characterization of Evaporation and Boiling From Sintered Powder Wicks Fed by Capillary Action," Int. J. Heat Mass Transfer, **53**(19–20), pp. 4204–4215.
[5] Wang, C., Liu, Z., Zhang, G., and Zhang, M., 2013, "Experimental Investigations of Flat Plate Heat Pipes With Interlaced Narrow Grooves or Channels as Capillary Structure," Exp. Therm. Fluid Sci., **48**, pp. 222–229.
[6] Wong, S. C., Hsieh, K. C., Wu, J. D., and Han, W.-L., 2010, "A Novel Vapor Chamber and its Performance," Int. J. Heat Mass Transfer, **53**(11–12), pp. 2377–2384.
[7] Xuan, Y., Hong, Y., and Li, Q., 2004, "Investigation on Transient Behaviors of Flat Plate Heat Pipes," Exp. Therm. Fluid Sci., **28**(2–3), pp. 249–255.
[8] Chen, Y. T., Kang, S. W., Hung, Y. H., Huang, C. H., and Chien, K. C., 2013, "Feasibility Study of an Aluminum Vapor Chamber With Radial Grooved and Sintered Powders Wick Structures," Appl. Therm. Eng., **51**(1–2), pp. 864–870.
[9] Mochizuki, M., Saito, Y., Kiyooka, F., Nguyen, T., Nguyen, T., and Wuttijumnong, V., 2007, "Advanced Micro-Channel Vapor Chamber for Cooling High Power Processors," ASME Paper No. IPACK2007-33611.
[10] Hwang, G. S., Nam, Y., Fleming, E., Dussinger, P., Ju, Y. S., and Kaviany, M., 2010, "Multi-Artery Heat Pipe Spreader: Experiment," Int. J. Heat Mass Transfer, **53**(13–14), pp. 2662–2669.
[11] Koito, Y., Imura, H., Mochizuki, M., Saito, Y., and Torii, S., 2006, "Numerical Analysis and Experimental Verification on Thermal Fluid Phenomena in a Vapor Chamber," Appl. Therm. Eng., **26**(14–15), pp. 1669–1676.
[12] Moritz, A. R., and Henriques, F. C., Jr., 1947, "Studies of Thermal Injury II: The Relative Importance of Time and Surface Temperature in the Causation of Cutaneous Burns," Am. J. Pathol., **23**(5), pp. 695–720.
[13] Berhe, M. K., 2007, "Ergonomic Temperature Limits for Handheld Electronic Devices," ASME Paper No. IPACK2007-33873.
[14] NASA JPL, 2012, "NASA Master Paints," NASA Jet Propulstion Laboratory, California Institute of Technology, Pasadena, CA, http://masterweb.jpl.nasa.gov/reference/paints.htm
[15] ANSYS, 2011, ANSYS FLUENT 14.0: User's Guide, Ansys Inc., Canonsburg, PA.
[16] Yadavalli, Y., Weibel, J. A., and Garimella, S. V., 2015, "Performance-Governing Transport Mechanisms for Heat Pipes at Ultrathin Form Factors," IEEE Trans. Compon. Packag. Manuf. Technol., **5**(11), pp. 1618–1627.